Angular Spread Quantification of Multi-Antenna Vehicular Radio Communication Channels

Abrar Ahmed*, Syed Junaid Nawaz*, Sardar Muhammad Gulfam*, Shurjeel Wyne*, Mohammad N. Patwary†, and Haris Pervaiz§.

*Department of Electrical Engineering, COMSATS University Islamabad, Islamabad, Pakistan.
†School of Computing and Digital Technology, Birmingham City University, Birmingham, UK.
§5G Innovation Centre, Faculty of Engineering and Physical Sciences, University of Surrey, UK.

abrar_ahmed@comsats.edu.pk, *junaidnawaz@ieee.org*, *sardar_muhammad@comsats.edu.pk*, *shurjeel.wyne@comsats.edu.pk*, *mohammad.patwary@bcu.ac.uk*, and *h.pervaiz@surrey.ac.uk*

***Abstract*—The deployment of multi-antenna systems with software defined reconfigurable beam patterns can potentially benefit vehicle-to-vehicle (V2V) communications by increasing the channel coherence time. This in turn necessitates an accurate characterization and modeling of the angular statistics of vehicular radio propagation environments. This work proposes an improved three-dimensional (3-D) spatial description of vehicular propagation environments and derives the closed-form analytical expressions for the joint and marginal statistics of the 3-D angle-of-arrival (AoA) and angle-of-departure (AoD). Then, based on the proposed geometric channel model, the AoA and AoD angular spreads are quantified in terms of the joint angular spread, elevational constriction, and the azimuthal constriction. These considered quantifiers are shown to be of high significance in quantification of angular spread in V2V radio propagation environments. The impact of various physical parameters on the angular spread is also investigated. These parameters include the link-distance, scattering volume, and the number of scatterers along the azimuth and elevation axes. The derived analytical expressions are also validated by simulations.**

Keywords: Angular spread, vehicle-to-vehicle, directional antennas, geometric modeling

I. Introduction

The deployment of directional antennas with software defined reconfigurable beam patterns in vehicle-to-vehicle (V2V) communication systems has a strong potential in enhancing the link capacity [1]. V2V communications is an emerging paradigm of communication networks with applications in intelligent transport systems (ITS) and urban traffic management [2, 3]. The V2V radio propagation channels are different in many aspects from the widely studied land mobile cellular communication channels [4, 5]. The mobility at both communicating nodes and a typically low altitude of the antennas surrounded by rich scattering makes the V2V communication channels highly time-variant. The large angular spread in such mobility scenarios imposes a high Doppler spread, which translates to a fast time-variability of the channel and a reduced channel coherence time. However, highly directional antennas can be deployed at both ends of the link to potentially reduce the spatial spread and thereby increase the channel coherence time. Designing of such software controlled reconfigurable directional antenna beams necessitate an accurate spatial description of the V2V radio propagation environments. Such modeling of the propagation environment is also of vital importance in characterizing the channel fading statistics.

Recently, the deployment of massive multiple-input multiple-output (MIMO), a key enabling technology for the 5-th generation (5G) of mobile communication systems, has been advocated for V2V communication systems [5, 6]. Apart from providing advantages of spatial multiplexing and/or diversity, these large antenna arrays can help to achieve optimal thin beams, which in turn can increase the channel coherence time. This solution becomes more valuable for communication over radically higher frequency bands (mmWave bands) [7, 8]; this is because the high carrier frequency in mmWave band linearly scales the Doppler shift of each multipath leading to higher Doppler spread even in low mobility conditions. The demands for consideration of spatial consistency and spherical wavefront in modeling the massive-MIMO communication channels makes it different from the requirements in modeling conventional MIMO channels [9]. In this context, various channel models considering spherical wavefront and/or channel non-stationarity have been proposed in the literature, see e.g., [10–13]. In [6], the channel's spatio-temporal non-stationarity for WINNER II and Saleh-Valenzuela models is studied for their applicability in V2V communication scenarios. In [14], a thorough comparative study on the applicability of various existing models for massive-MIMO systems is conducted and the COST 2100, METIS, and IEEE 802.11ad models are suggested as suitable choices. Geometry-based stochastic modeling of the wireless communication channels offers the advantages of generality and provision of closed-form analytical expression for establishing the probabilistic relationship between the spatial location of transmitter, receiver, and scattering objects. In various vehicular radio propagation environments (e.g., streets, highways, merging/spliting lanes, flyovers, etc), the scatterers are usually absent in the immediate vicinity of the vehicular nodes; therefore, various geometric models model the scattering region in close vicinity of vehicular nodes as a scatterer-free region, see e.g., [4, 15, 16]. A

Dual annular strip model is proposed in [16], where analytical expressions for the probability distribution function (PDF) of the Angle-of-Arrival (AoA) in V2V communication scenarios is derived. In [5], a geometric channel model for V2V massive-MIMO communications is presented by considering the PDF of both azimuth and elevation AoA as Gaussian. In [4, 7], a more realistic description of the scattering environments is presented for the characterization of angular statistics in massive-MIMO vehicular radio communication environments. Various other studies are also available in the literature which aim at defining the scattering volumes as realistic yet simple enough to keep the advantages of the model's tunability and generality, see e.g., [17–19]. In this quest for an accurate, tuneable, and generalized 3-D spatial description of scattering volumes in the vicinity of communication nodes, there is a significant scope to conduct intensive research work. Such studies can be of high significance for characterization of the Doppler spectrum, second-order fading statistics, and optimal beam designing in vehicular radio communication environments.

Quantification of the joint 3-D angular spread at transmitter and receiver side is of vital importance in enabling the employment of massive-MIMO in V2V communication systems. In [20], spatial spread quantifiers for vehicle-to-vehicle radio propagation environments are proposed, however the presented analysis is conducted for over simplified geometry of the scattering clusters. In this paper, a geometry based generalized and tunable 3-D stochastic model is presented for V2V communication environments. Analytical expressions for the joint and marginal 3-D description of AoA and angle-of-departure (AoD) are derived. A thorough analysis of the impact of various physical channel parameters on spatial statistics of vehicular propagation environments is conducted. Analysis is further extended from plain angular statistics to the quantification of angular spread in azimuth and elevation planes for both transmitting and receiving sides of the link.

The remainder of this paper is organized as follows. In Section II, the proposed channel model is presented. Section III provides the derivations of the analytical expressions for the joint and marginal PDFs of AoA and AoD and the definitions of the considered angular spread quantifiers is also presented. In Section IV, some results and discussion along with the validation of the analysis is provided. Finally, the conclusion is presented in Section V.

II. Geometry of Scattering Clusters

This section presents the description of proposed 3-D geometrically based V2V channel model. The effective scattering region is defined as confined within the non overlapping region of an inner-bounding elliptical-cylindric and outer-bounding ellipsoidal shaped volumes centered at the position of each mobile station (MS). The scattering objects are assumed to be uniformly distributed within the defined scattering volumes located around each vehicular node. The considered geometric composition of the scattering volumes in illustrated in Fig. 1. Both the vehicular nodes are separated by a horizontal distance d. The outer and inner boundaries of the scattering

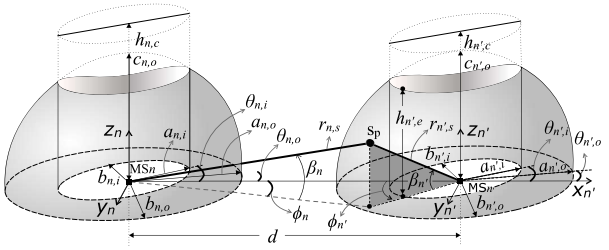

Fig. 1. Geometry of 3-D scattering regions in V2V communications.

clusters around the vehicular nodes are modeled as ellipsoidal and elliptic-cylinder, respectively. These geometric shapes modeling the boundaries of the scattering volumes are labeled as $E_{n,k}$, where the subscripts k and n represents the scattering region's boundary k (inner or outer) around n^{th} MS. The index k takes the label as $k = o$ and $k = i$ to represent the outer and inner boundary, respectively. The outer bounding ellipsoids around each MS (e.g., MSn) is modeled as independently scalable along x-, y-, and z-axis with the parameters $a_{n,o}$, $b_{n,o}$, and $c_{n,o}$, respectively. The outer and inner boundary of the scattering volumes around a MS$n/n'$ is modeled as rotatable in x-y plane with an angle $\theta_{n/n',i/o}$. In typical outdoor vehicular radio propagation scenarios, the arrival of signals from the elevation angles around 90° is unlikely, this is because of the absence of any scatterers in the directions right above the MSs, this motivates the modeling of inner boundary of scattering volumes as hollow cylindric region. Major and minor axis of the elliptical cylinders are represented by $a_{n,i}$ and $b_{n,i}$, respectively. The inner bounding cylinders are taken of height $h_{n,c}$ to be more than minor axis of outer bounding ellipsoid $c_{n,o}$. The inner elliptical-cylindric shaped boundary is also modeled as rotatable in azimuth plane with angle $\theta_{n,i}$. The scattering volumes in the proposed system can effectively adapt to model various communication environments and scenarios with the provided seven degrees-of-freedom ($\theta_{n,o}$, and $\theta_{n,i}$, $a_{n,i}$, $b_{n,i}$, $a_{n,o}$, $b_{n,o}$, $c_{n,o}$.). This flexibility in the shape of scattering volumes can also help in studying the channel characteristics in various dynamic scenarios, including V2V communications. The position of a certain MS can be represented by (x_n, y_n, z_n) in the Cartesian coordinate system. The outer bounding ellipsoids around MSn can thus be defined as,

$$\frac{((x_{n,k}-x_n)\cos\theta_{n,k}+(y_{n,k}-y_n)\sin\theta_{n,k})^2}{a_{n,k}^2}+\frac{(z_{n,k}-z_n)^2}{c_{n,k}^2} +\frac{(-(x_{n,k}-x_n)\sin\theta_{n,k}+(y_{n,k}-y_n)\cos\theta_{n,k})^2}{b_{n,k}^2}=1. \tag{1}$$

The spatial position of MSn and MSn' at a temporal snap is taken as $(0,0,0)$ and $(d,0,0)$, respectively. Following are some important relationships, which are later used in the applied transformations: $x_n = r_n\cos\beta_n\cos\phi_n$, $y_n = r_n\cos\beta_n\sin\phi_n$, $z_n = r_n\sin\beta_n$, $x_{n'} = x_n + d$, $y_{n'} = y_n$, and $z_{n'} = z_n$. The azimuth and elevation AoA is represented by ϕ_n and β_n, respectively. The volume V_n of scattering region around MSn is obtained by subtracting the volume of inner

cylinder $V_{\mathrm{n,i}}$ from the volume of outer ellipsoid $V_{\mathrm{n,o}}$, i.e., $V_n = V_{\mathrm{n,o}} - V_{\mathrm{n,i}}$. V_n is obtained as,

$$V_n = \tfrac{2}{3}\pi a_{n,o} b_{n,o} c_{n,o} - 2\int_0^{\gamma_m} \frac{c_{\gamma n,o}}{a_{\gamma n,o}} \int_{\eta_l^-}^{\eta_u^+} \sqrt{{a_{\gamma n,o}}^2 - \eta^2}\ \mathrm{d}\eta\ \mathrm{d}\gamma, \quad (2)$$

where η represents the dimension of an arbitrary horizontal plane along x-axis, in parallel to y-z plane. The parameter γ represents the length of scattering region along y-axis, parallel to the x-z plane. Closed-form solution for the volume of a single scattering cluster can be obtained, as derived in [19] for similar geometry in fixed-to-vehicle communication context. Total volume of illuminated scattering region can thus be represented as $V_e = V_n + V_{n'}$. As illustrated in Fig. 2, the important azimuth threshold angles, separating among different regions of the scattering volumes with different geometric compositions, can be derived as,

$$\phi_{n,k}^{\pm} = \arctan\Bigg\{ \frac{(a_{n,k}^2 - b_{n,k}^2)\cos\theta_{n,k}\sin\theta_{n,k}}{a_{n,k}^2\cos^2\theta_{n,k} + b_{n,k}^2\sin^2\theta_{n,k} - d^2} \pm\big\{d^2(a_{n,k}^2\sin^2\theta_{n,k} + b_{n,k}^2\cos^2\theta_{n,k}) - a_{n,k}^2 b_{n,k}^2\big\}^{\frac{1}{2}} \Bigg\}. \quad (3)$$

An azimuth threshold angle represent a particular azimuth direction of observation in which an extended line from MSn draws a tangent point at the outer or inner boundary of far-end (i.e., MSn') scattering volume, see Fig. 2. By setting $\mathrm{k} = i$ and $\mathrm{k} = o$ in (3), the azimuth threshold angles $\phi_{n,i}^{\pm}$ and $\phi_{n,o}^{\pm}$ can be drawn, respectively. Along the elevation axis, the effective portion of a scattering volume is divided into different angular partitions. The important elevation threshold angles to classify among these partitions are represented by $\beta_{n,1}$, $\beta_{n,2}$, $\beta_{n,3}$ and $\beta_{n,o}$, as shown in Fig. 3. Simplified expressions of the aforementioned angles is given below,

$$\left.\begin{matrix}\beta_{n,1}^- \\ \beta_{n,2}^+\end{matrix}\right\} = \arctan\left(\frac{h_{n',e}^{\mp}}{\rho_{\phi n,i}^{\mp}}\right). \quad (4)$$

Observing in a specific direction (ϕ_n and β_n), the parameters $h_{n',e}^{\pm}$ of inner cylinder can be expressed as,

$$h_{n',e}^{\pm} = \frac{c_{n',o}}{a_{n',o}b_{n',o}}\Bigg\{\frac{1}{2}(a_{n',o}^2(2b_{n',o}^2 - d^2 - {\rho_{\phi n,i}^{\pm}}^2) - b_{n',o}^2(d^2 + {\rho_{\phi n,i}^{\pm}}^2) + (a_{n',o}^2 - b_{n',o}^2)\cos(2(\alpha - \theta_{n',o})) \times(d^2 + {\rho_{\phi n,i}^{\pm}}^2 - 2d\rho_{\phi n,i}^{\pm}\cos\phi_n))\Bigg\}^{\frac{1}{2}}, \quad (5)$$

where,

$$\alpha = \pi - \arcsin\left(\frac{\rho_{\phi n,i}^{\pm}\sin\phi_n}{\sqrt{d^2 + {\rho_{\phi n,i}^{\pm}}^2 - 2d\rho\cos\phi_n}}\right). \quad (6)$$

When observing from MSn in a given direction, the height of local-end cylindric wall is shown by $h_{n,e}$, while the maximum elevation angle formed with the line is $\beta_{n,3}$, see Fig. 3. These parameters can be expressed as,

$$h_{n,e} = c_{n,o}\sqrt{\frac{4a_{n,o}^4 b_{n,o}^4 - r_{n,i}^2\cos^2\beta_n (g_{n,o})^2}{2a_{n,o}^2 b_{n,o}^2 (g_{n,o})}}, \quad (7)$$

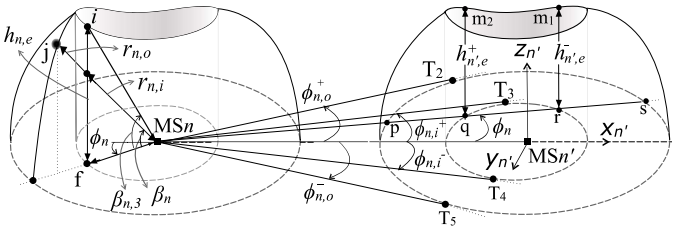

Fig. 2. Important azimuth threshold angles of the proposed scattering model.

and

$$\beta_{n,3} = \arctan\left(\frac{h_{n,e}}{r_{n,i}\cos\beta_n}\right), \quad (8)$$

where,

$$g_{n,o} = a_{n,o}^2 + b_{n,o}^2 + (-a_{n,o}^2 + b_{n,o}^2)\cos 2(\theta_{n,o} - \phi_n). \quad (9)$$

Another important threshold angle indicated in Fig. 3 is $\beta_{n,o}$. It represents the elevation angle made with the line drawn from the MSn at a particular azimuth angle to the tangent point formed at the outer bounding ellipsoid around the MSn' (far-end), which can be represented by,

$$\beta_{n,o} = \begin{cases} \arctan\left(\dfrac{2c_{\phi,n}}{\sqrt{(\rho_{\phi_{n,o}}^+ + \rho_{\phi_{n,o}}^-)^2 - 4a_{\phi,n}^2}}\right) & ;\phi_{n,o}^- \le \phi_n \le \phi_{n,o}^+ \\ 0 & ;\ \text{otherwise.}\end{cases} \quad (10)$$

In a given particular direction of observation from MSn, the parameters $r_{n,i}$ and $r_{n,o}$ represent the distance from MSn to the nearest (at inner surface) and farthest (at outer surface) of the scattering cluster around MSn, respectively. These distances can be expressed in simplified form as,

$$r_{n,i} = \frac{1}{\cos\beta_n}\sqrt{\frac{2a_{n,i}^2 b_{n,i}^2}{a_{n,i}^2 + b_{n,i}^2 + (b_{n,i}^2 - a_{n,i}^2)\cos 2(\theta_{n,i} - \phi_n)}}, \quad (11)$$

$$r_{n,o} = \big\{a_{n,o}^2 b_{n,o}^2\sin^2\beta_n + a_{n,o}^2\sin^2(\theta_{n,o} - \phi_n) + c_{n,o}^2\cos^2\beta_n(b_{n,o}^2\cos^2(\theta_{n,o} - \phi_n))\big\}^{-\frac{1}{2}} a_{n,o}b_{n,o}c_{n,o} \quad (12)$$

For the elevation angle fixed at $\beta_n = 0°$, the horizontal distances from MSn, at a particular azimuth angle ϕ_n, to the intersection points p and s with outer bounding ellipsoid and q and r with inner cylindric boundary are represented by $\rho_{\phi_{n,k}}^{\pm}$, see Fig. 3, which can be expressed as,

$$\left.\begin{matrix}\rho_{\phi_{n,k}}^+ \\ \rho_{\phi_{n,k}}^-\end{matrix}\right\} = \frac{-1}{a_{n,k}^2 + b_{n,k}^2 + (b_{n,k}^2 - a_{n,k}^2)\cos(2(\theta_{n,k} - \phi_n))}\Big\{2d(b_{n,k}^2\cos\theta_{n,k} \times\cos(\theta_{n,k} - \phi_n) + a_{n,k}^2\sin\theta_{n,k}\sin(\theta_{n,k} - \phi_n)) \pm\Big(2a_{n,k}^2 b_{n,k}^2\cos^2\phi_n(a_{n,k}^2 + b_{n,k}^2 - d^2 + (b_{n,k}^2 - a_{n,k}^2)\cos(2(\theta_{n,k} - \phi_n)) + d^2\cos(2\phi_n))\Big)^{\frac{1}{2}}\Big\}, \quad (13)$$

The simplification parameters, can be defined as,

$$c_{\phi,n} = -\frac{c_{n',o}}{a_{n',o}b_{n',o}} \times\sqrt{a_{n',o}^2 b_{n',o}^2 - a_{n',o}^2 x_{n,e}^2\sin^2\theta_{n,e} - b_{n',o}^2 x_{n,e}^2\cos^2\theta_{n,e}}, \quad (14)$$

$$a_{\phi,n} = \frac{1}{(a^2_{n',o} + b^2_{n',o} + (b^2_{n',o} - a^2_{n',o})\cos 2(\theta_{n',o} - \phi_n))\cos\phi_n} \times \Big\{ -2a^2_{n',o} b^2_{n',o} \cos^2\phi_n (d^2 - a^2_{n',o} - b^2_{n',o} + (a^2_{n',o} - b^2_{n',o})\cos 2(\theta_{n',o} - \phi_n) - d^2\cos 2\phi_n) \Big\}^{\frac{1}{2}}, \quad (15)$$

$$x_{n,e} = \sqrt{d^2 + (a_{\phi,n} + \rho^+_{\phi n,o})^2 - 2d(a_{\phi,n} + \rho^+_{\phi n,o})\cos\phi_n}, \quad (16)$$

$$\theta_{n,e} = \begin{cases} \pi - (\theta_{n,r} + \theta_{n,o}) & ; \ \phi_n < 0°, \\ \theta_{n,r} + \theta_{n,o} & ; \ \text{otherwise}, \end{cases} \quad (17)$$

and

$$\theta_{n,r} = \begin{cases} \arcsin\left(\dfrac{a_{\phi,n} + \rho^+_{\phi n,o}}{x_{n,e}\csc\phi_n}\right) & ; \ \phi_n \neq 0, \\ 0 & ; \ \phi_n = 0°. \end{cases} . \quad (18)$$

In a particular direction of observation from MSn, the distances to the intersection points t, w and u, v formed at inner and outer boundary of the far-end cluster is represented by $\rho^{\pm}_{\beta n,o}$ and $\rho^{\pm}_{\beta n,i}$. These parameters can be expressed as,

$$\left.\begin{matrix} \rho^+_{\beta n,o} \\ \rho^-_{\beta n,o} \end{matrix}\right\} = \sec\beta_n \Big\{ \frac{1}{a^2_{\phi,n} + c^2_{\phi,n} + (c^2_{\phi,n} - a^2_{\phi,n})\cos(2\beta_n)} \Big((a_{\phi,n} + \rho^+_{\phi n,o}) - \big(2a^2_{\phi,n}\sin\beta_n((a_{\phi,n} + \rho^+_{\phi n,o})\sin\beta_n) \pm (2(a^2_{\phi,n}c^2_{\phi,n}\cos^2\beta_n(a^2_{\phi,n} + c^2_{\phi,n} - (a_{\phi,n} + \rho^+_{\phi n,o})^2 + (c^2_{\phi,n} - a^2_{\phi,n} + (a_{\phi,n} + \rho^+_{\phi n,o})^2)\cos(2\beta_n))))^{\frac{1}{2}}\big) \Big) \Big\}, \quad (19)$$

$$\rho^{\pm}_{\beta_{n,i}} = \rho^{\pm}_{\phi_{n,i}} \sec\beta_n. \quad (20)$$

When observing from a certain vehicular node (e.g., MSn) the effective scattering region can be partitioned into four angular partitions based on the geometric composition of the regions. Using the defined threshold azimuth and elevation angles, the angular partitions can be defined as,

$$\left\{ \ \phi^-_{n,i} < \phi_n < \phi^+_{n,i} \ \text{ and } \ 0 \leq \beta_n \leq \beta_{n,1} \ \right\} \rightarrow P_{n,1}, \quad (21)$$

$$\left\{ \ \phi^-_{n,i} < \phi_n < \phi^+_{n,i} \ \text{ and } \ \beta_{n,1} \leq \beta_n \leq \beta_{n,2} \ \right\} \rightarrow P_{n,2}, \quad (22)$$

$$\left\{ \begin{matrix} \{\phi^+_{n,i} < \phi_n < \phi^+_{n,o} \ \text{ or } \ \phi^-_{n,o} < \phi_n < \phi^-_{n,i}\} \\ \text{and} \\ 0 \leq \beta_n \leq \beta_{n,o} \end{matrix} \right\} \rightarrow P_{n,3}, \quad (23)$$

$$\left\{ \ \phi^+_{n,o} < \phi_n < \phi^-_{n,o} \ \text{ and } \ \beta_{n,o} \leq \beta_n \leq \beta_{n,3} \ \right\} \rightarrow P_{n,4}. \quad (24)$$

III. Spatial Spread Statistics

In this section, PDFs of AoD and AoA in azimuthal and elevational planes have been presented. Considering a single bounce scenario, the arrival of signal at MSn from a given direction of arrival (ϕ_n, β_n) is only likely, if the line drawn in this direction intersects with the line drawn from the far-end MSn' in a given direction of departure $(\phi_{n'}, \beta_{n'})$ and the intersection point lies within the defined effective scattering region. This proposition helps in defining the 3-D joint PDF

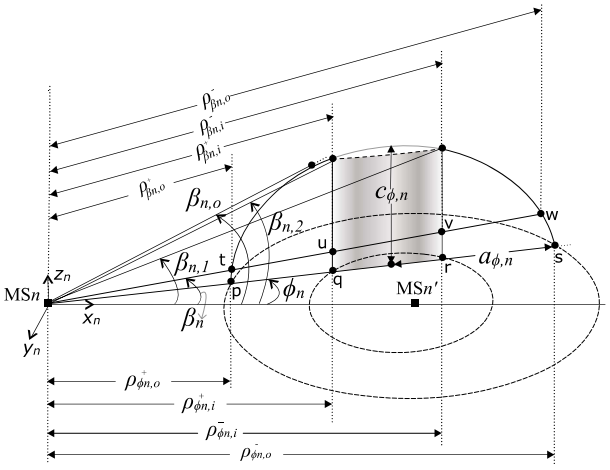

Fig. 3. Cross-section view of the scattering clusters.

of AoA and AoD as given below,

$$f(\phi_n, \beta_n, \phi_{n'}, \beta_{n'}) = \begin{cases} \dfrac{1}{V_e} & ; r_{n,i} \leq \dfrac{d\sin\phi_{n'}}{\sin(\phi_{n'} - \phi_n)\cos\beta_n} \leq r_{n,o}, \\ & \text{or} \\ & r_{n',i} \leq \dfrac{d\sin\phi_n}{\sin(\phi_{n'} - \phi_n)\cos\beta_{n'}} \leq r_{n',o}, \\ \dfrac{j_1}{V_e} & ; \phi_n = \beta_n = \phi_{n'} = \beta_{n'} = 0^o, \\ \dfrac{j_2}{V_e} & ; \phi_n = \beta_n = \beta_{n'} = 0^o, \phi_{n'} = 180^o, \\ \dfrac{j_3}{V_e} & ; \phi_n = \phi_{n'} = 180^o, \beta_n = \beta_{n'} = 0^o, \\ 0 & ; \text{otherwise}, \end{cases} \quad (25)$$

where the simplification parameters can be expressed as, $j_1 = \rho^-_{\beta n,o} - \rho^-_{\beta n,i}$, $j_2 = r_{n,o} - r_{n,i} + \rho^+_{\beta n,i} - \rho^+_{\beta n,o}$, $j_3 = r_{n,o} - r_{n,i}$. By integrating the density function $f(\phi_n, \beta_n, \phi_{n'}, \beta_{n'})$ over an appropriate set of parameters for their defined range, closed-from expression for the joint PDF of AoA observed at MSn can be expressed as,

$$p(\phi_n, \beta_n) = \begin{cases} \dfrac{\{(r_{n,o} - r_{n,i}) + (\rho^-_{\beta n,o} - \rho^-_{\beta n,i}) + (\rho^+_{\beta n,i} - \rho^+_{\beta n,o})\}^3\cos\beta_n}{3V_e} & ; P_{n,1}, \\ \dfrac{\{(r_{n,o} - r_{n,i}) + (\rho^+_{\beta n,i} - \rho^+_{\beta n,o})\}^3\cos\beta_n}{3V_e} & ; P_{n,2}, \\ \dfrac{\{(r_{n,o} - r_{n,i}) + (\rho^-_{\beta n,o} - \rho^+_{\beta n,o})\}^3\cos\beta_n}{3V_e} & ; P_{n,3}, \\ \dfrac{(r_{n,o} - r_{n,i})^3\cos\beta_n}{3V_e} & ; P_{n,4}. \end{cases} \quad (26)$$

Marginal PDF of azimuth and elevation AoA and AoD can be obtained by integrating (26) over appropriate parameters, e.g., the marginal PDF of azimuth AoA can be obtained as, $p(\phi_n) = \int_0^{\pi/2} p(\phi_n, \beta_n) d\beta_n$. The joint beam pattern of transmitter and receiver side antennas can be represented by $G(\phi_n, \beta_n, \phi_{n'}, \beta_{n'})$. Therefore, the joint angular power spectrum can be given as,

$$p(\phi_n, \beta_n, \phi_{n'}, \beta_{n'}) = f(\phi_n, \beta_n, \phi_{n'}, \beta_{n'}) G(\phi_n, \beta_n, \phi_{n'}, \beta_{n'}). \quad (27)$$

Since the antennas of transmitter and receiver are independent of each other, so the joint beam pattern can be expressed as $G(\phi_n, \beta_n, \phi_{n'}, \beta_{n'}) = G(\phi_n, \beta_n)G(\phi_{n'}, \beta_{n'})$. The beam pattern can be assumed as Gaussian shaped [21], for the purpose of achieving mathematical simplicity. The Gaussian shaped antenna gain function for MSn can be written as,

$$G(\phi_n, \beta_n) = \exp\left(-\frac{(\phi_n - \mu_{\phi_n})^2}{\sigma_{\phi_n}^2} - \frac{(\beta_n - \mu_{\beta_n})^2}{\sigma_{\beta_n}^2}\right), \quad (28)$$

where μ_{ϕ_n} and μ_{β_n} represent the angle at which the peak (mean) of the beam is pointed in azimuth and elevation planes, respectively; while $\sigma_{\phi_n}^2$ and $\sigma_{\beta_n}^2$ represent the width (standard deviation) of the beams in azimuth and elevation planes, respectively. This multiplicative factor of antennas directional gain overshadows the impact of various important fine details in the angular statistics caused by various physical channel parameters. Since the focus of this paper is mainly on investigating the behavior of transformation in shape, size, and orientation of the scattering clusters on the joint 3-D spatial spread, therefore the gain function is assumed as unity in all the directions, i.e., $G(\phi_n, \beta_n) = 1$. For quantification of energy dispersion in 2-D (angular) domain, a theory of multipath shape factors is proposed in [22]. This theory is extended in [20] for quantification of spatial spread in 3-D for fixed-to-vehicle and 6-D (i.e., 3-D AoA and 3-D AoD) for V2V channels. Among the proposed quantifiers for spatial spread in V2V propagation environments, the notable are joint angular spread (Υ), azimuthal constriction (ξ), and elevational constriction (ζ), which are defined as,

$$\Upsilon_n = \sqrt{1 - \frac{S_{1,0}^{0,0^2} + |S_{1,0}^{1,0}|^2}{S_{0,0}^{0,0^2}}}, \ \Upsilon_{n'} = \sqrt{1 - \frac{S_{0,1}^{0,0^2} + |S_{0,1}^{0,1}|^2}{S_{0,0}^{0,0^2}}}, \quad (29)$$

$$\xi_n = \frac{\frac{3}{2}S_{2,0}^{0,0}S_{0,0}^{0,0} - \left(S_{1,0}^{0,0^2} - \frac{1}{2}|S_{1,0}^{1,0}|^2\right)}{S_{0,0}^{0,0^2} - \left(S_{1,0}^{0,0^2} + |S_{1,0}^{1,0}|^2\right)}, \ \xi_{n'} = \frac{\frac{3}{2}S_{0,2}^{0,0}S_{0,0}^{0,0} - \left(S_{1,0}^{0,0^2} - \frac{1}{2}|S_{1,0}^{1,0}|^2\right)}{S_{0,0}^{0,0^2} - \left(S_{1,0}^{0,0^2} + |S_{1,0}^{1,0}|^2\right)}, \quad (30)$$

$$\zeta_n = \frac{|S_{2,0}^{2,0}S_{0,0}^{0,0} - S_{1,0}^{1,0^2}|}{S_{0,0}^{0,0^2} - \left(S_{1,0}^{0,0^2} + |S_{1,0}^{1,0}|^2\right)}, \ \zeta_{n'} = \frac{|S_{0,2}^{0,2}S_{0,0}^{0,0} - S_{1,0}^{1,0^2}|}{S_{0,0}^{0,0^2} - \left(S_{1,0}^{0,0^2} + |S_{1,0}^{1,0}|^2\right)}. \quad (31)$$

The joint angular spread, ranges from 0 to 1; with the value 0 representing the energy concentrated in one physical direction, whereas 1 showing no clear bias. Elevational constriction ranges from -0.5 to 1, with the value of -0.5 indicating the arrival of signals concentrated around single elevational cone and 1 representing the arrival of signals from exactly opposite elevational angle at the same azimuthal angle. The azimuthal constriction ranges from 0 to 1, with the value of 1 representing the signal arriving from two different physical paths from same elevation angle and its value 0 represent no clear bias. The important double spherical harmonic coefficients $S_{s,l}^{m,p}$ can be computed as,

$$S_{s,l}^{m,p} = \int_{-\pi}^{\pi}\int_{0}^{\frac{\pi}{2}}\int_{-\pi}^{\pi}\int_{0}^{\frac{\pi}{2}} p(\phi_n, \beta_n, \phi_{n'}, \beta_{n'}) \times W_{s,l}^{m,p*} \cos\beta_n \cos\beta_{n'} \mathrm{d}\beta_n \mathrm{d}\beta_{n'} \mathrm{d}\phi_n \mathrm{d}\phi_{n'}. \quad (32)$$

The simplification parameters $W_{s,l}^{m,p}$ are given as below,

$$W_{0,0}^{0,0} = 1, W_{1,1}^{0,0} = \sin\beta_n \sin\beta_{n'}, W_{1,0}^{0,0} = \sin\beta_n,$$
$$W_{0,1}^{0,0} = \sin\beta_{n'}, W_{1,1}^{0,1} = \cos\beta_{n'} \mathrm{e}^{j\phi_{n'}} \sin\beta_n,$$
$$W_{1,1}^{1,0} = \cos\beta_n \mathrm{e}^{j\phi_n} \sin\beta_{n'}, W_{1,1}^{1,1} = \cos\beta_n \cos\beta_{n'} \mathrm{e}^{j(\phi_n + \phi_{n'})},$$
$$W_{0,2}^{0,2} = \cos^2\beta_{n'} \mathrm{e}^{j2\phi_{n'}}, W_{2,0}^{2,0} = \cos^2\beta_n \mathrm{e}^{j2\phi_n},$$
$$W_{1,0}^{1,0} = \cos\beta_n e^{j\phi_n}, W_{0,1}^{0,1} = \cos\beta_{n'} \mathrm{e}^{j\phi_{n'}}, W_{2,0}^{1,0} = \sin 2\beta_n \mathrm{e}^{j\phi_n},$$
$$W_{2,0}^{0,0} = 2\sin^2\beta_n - \frac{2}{3}, W_{0,2}^{0,0} = 2\sin^2\beta_{n'} - \frac{2}{3},$$
$$W_{0,2}^{0,1} = \sin 2\beta_{n'} \mathrm{e}^{j\phi_{n'}}, W_{1,1}^{1,-1} = \cos\beta_n \cos\beta_{n'} \mathrm{e}^{j(\phi_n - \phi_{n'})}.$$

IV. Results and Discussion

A comprehensive analysis on obtained analytical results of spatial statistics for V2V radio communication channels is presented. Validation of proposed geometric model is achieved by comparing the with computer simulation results. In the predefined regions around both communication vehicular nodes the scattering clusters are created. Scatterers are distributed uniformly in these clusters. Adopting the methodology proposed in [19], the PDFs of the azimuthal and elevational AoA calculated for simulation results. A very good match between the simulation and analytical results can be observed in Fig. 4; these results are obtained for 100 uniformly distributed scattering objects in each cluster and after 10^4 Monte Carlo runs. This good match demonstrates the validity of derived analytical expressions.

The results obtained for the PDF of azimuth and elevation AoA are taken by considering the MSn and MSn' as the receiver and transmitter, respectively. The impact of horizontal link distance d, MSn inner cylinder volume in terms of $a_{n,i}$ and $b_{n,i}$), and ratio between vertical dimensions of scattering volumes around MSn and MSn', on marginal PDF of the azimuthal and elevational AoA is plotted in Fig. 5 and 6, respectively. Effect of horizontal link distance between the communication nodes on marginal PDF of the azimuthal and elevational AoA is shown in Fig. 5(a) and 6(a), respectively. Other parameters of MSn are taken as $a_{n,i} = 45$m, $b_{n,i} = 25$m, $a_{n,o} = 75$m, $b_{n,o} = 65$m, $c_{n,o} = 65$m, and $\theta_{n,i} = \theta_{n,o} = 0^o$. The parameter of MS$n'$ are $a_{n',i} = 35$m, $b_{n',i} = 15$m, $a_{n',o} = 65$m, $b_{n',o} = 55$m, $c_{n',o} = 55$m, and $\theta_{n',i} = \theta_{n',o} = 0^o$. In Fig. 5(a) as the nodes come near each other, value for the peak of PDF seen around LoS path decreases with an increase in overall angular spread; this is because the contribution of far-end MSn' scattering cluster becomes more influential. This translates that an increase in the link distance causes a decrease in the contribution from far-end, thus the span of peak around LoS direction sharpens. Similar effect on the PDF of elevation AoA can also be observed in Fig. 6(a). An increase in the link distance causes an increase in the relative probability of signals arrival from the scattering volumes around observing-end MSn compared to the volume around far-end MSn'.

The impact of widening the scattering free region in the close vicinity of vehicular nodes is demonstrated in Fig. 5(b) and 6(b) on the PDF of azimuth and elevation AoA. In a typical vehicular propagation environment, the close vicinity of nodes is usually encountered as scattering free region, this

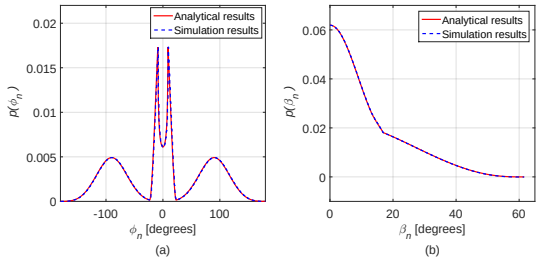

Fig. 4. Simulation and analytical results comparison for marginal PDF of (a) azimuth AoA and (b) elevation AoA, observing from MSn. ($a_{n,o}$ = 65m, $b_{n,o}$ = 85m, $c_{n,o}$ = 65m, $a_{n,i}$ = 55m, $b_{n,i}$ = 35m, $\theta_{n,o} = \theta_{n,i} = 0^o$. $a_{n',o}$ = 60m, $b_{n',o}$ = 40m, $c_{n',o}$ = 35m, $a_{n',i}$ = 25m, $b_{n',i}$ = 20m, $\theta_{n',o} = \theta_{n',i}$ = 0^o, and d = 110m).

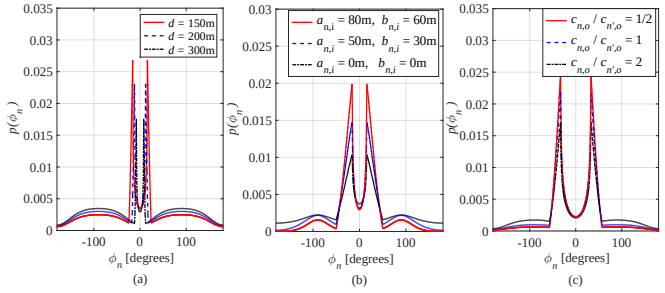

Fig. 5. Effect of (a) distance d between MSn and MSn', (b) size of inner cylinder ($a_{n,i}$ and $b_{n,i}$) of MSn, and (c) ratio of height of MSn and MSn', on marginal PDF of azimuth AoA as seen from MSn

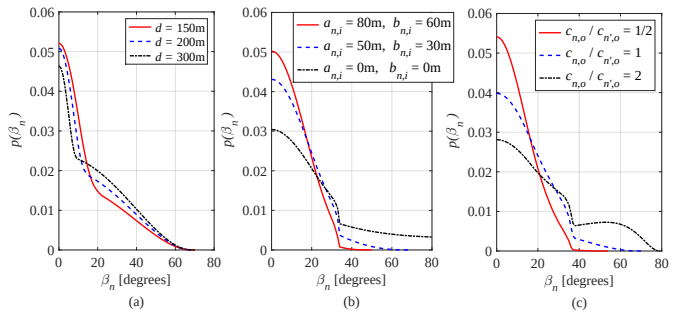

Fig. 6. Effect of (a) distance d between MSn and MSn', (b)inner cylinder's size ($a_{n,i}$ and $b_{n,i}$) of MSn, and (c) ratio of height of MSn and MSn', on marginal PDF of elevation AoA as seen from MSn

hollow region may thus represent the width of highway or street etc. The physical parameters of MSn taken for obtaining these graphs are $a_{n,o} = 100$m, $b_{n,o} = 150$m, $c_{n,o} = 80$m, and $\theta_{n,i} = \theta_{n,o} = 0^o$. Parameters of MS$n'$ are $a_{n',o} = 95$m, $b_{n',o} = 75$m, $c_{n',o} = 75$m, $a_{n',i} = 50$m, $b_{n',i} = 30$m, $\theta_{n',i} = \theta_{n',o} = 0^o$ and $d = 125$m. The volume of inner bounding cylinder is varied, and volume of ellipsoid is unchanged. In Fig. 5(b) it is evident that as the volume of scattering free region (cylindric) in the cluster around far-end increases, a dip in the PDF of AoA along the LoS direction is observed. In Fig. 6(b), it is evident that with the increase in volume of inner cylinder number of scatterers along the elevational plane for higher elevation angles decreases. This upper limit on elevation angle $\beta_{n,3}$ approaches to the maximum of $\pi/2$ with a decrease in hollow (scattering free) region, thus an

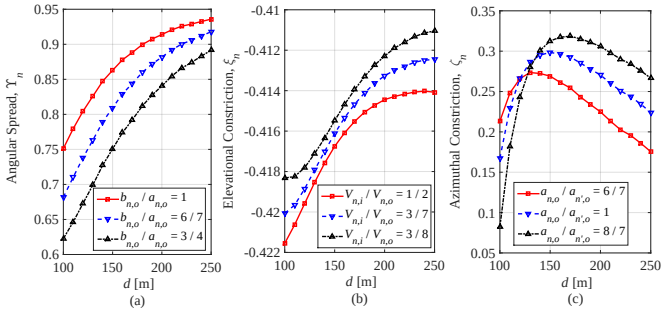

Fig. 7. Observing from MSn, the effect of variation in distance d between MSn and MSn' and, (a) ratio of intermediate and major axis of ellipsoid at the local end on angular spread is shown, $c_{n',o}$ = 60m, $b_{n',o}$ = 60m, $a_{n',o}$ = 70m, $b_{n',i}$ = 20m, $a_{n',i}$ = 30m, $c_{n,o}$ = 40m, $b_{n,i}$ = 20m, $a_{n,i}$ = 30m, $\theta_{n',i} = \theta_{n',o} = 0°$, (b) change in volume on elevational constriction is shown, $c_{n',o}$ = 60m, $b_{n',o}$ = 60m, $a_{n',o}$ = 70m, $b_{n',i}$ = 20m, $a_{n',i}$ = 30m, $b_{n,o}$ = 60m, $b_{n,i}$ = 20m, $c_{n,o}$ = 40m, $\theta_{n',i} = \theta_{n',o} = 0°$, (c) ratio of major axis of ellipsoid at the local and far end on azimuthal constriction is shown, $c_{n',o}$ = 60m, $b_{n',o}$ = 60m, $b_{n',i}$ = 20m, $c_{n',i}$ = 20m, $c_{n,o}$ = 40m, $b_{n,o}$ = 40m, $b_{n,i}$ = 20m, $a_{n,i}$ = 30m, $\theta_{n',i} = \theta_{n',o} = 0°$.

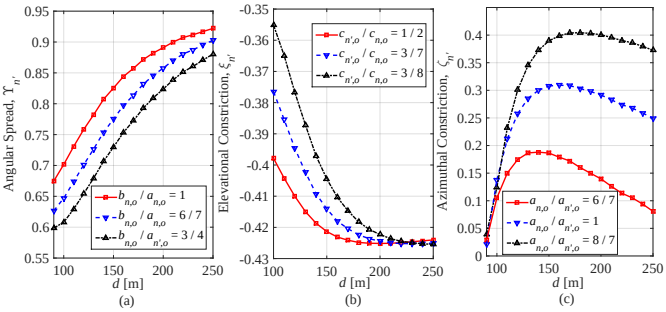

Fig. 8. Observing from MSn', the effect of variation in distance d between MSn and MSn' and, (a) ratio of intermediate and major axis of ellipsoid at the far end on angular spread is shown, $c_{n,o}$ = 60m, $b_{n,i}$ = 20m, $a_{n,i}$ = 30m, $c_{n',o}$ = 40m, $b_{n',o}$ = 60m, $a_{n',o}$ = 60m, $b_{n',i}$ = 20m, $a_{n',i}$ = 30m, $\theta_{n',i} = \theta_{n',o} = 0°$, (b) ratio of height of ellipsoids on elevational constriction is shown, $b_{n,o}$ = 60m, $a_{n,o}$ = 70m, $b_{n,i}$ = 20m, $a_{n,i}$ = 30m, $b_{n',o}$ = 60m, $a_{n',o}$ = 60m, $b_{n',i}$ = 20m, $a_{n',i}$ = 30m, $\theta_{n'i} = \theta_{n',o} = 0°$, (c) ratio of major axis of ellipsoid at the far and local end on azimuthal constriction is shown, $c_{n,o}$ = 60m, $b_{n,o}$ = 60m, $b_{n,i}$ = 20m, $a_{n,i}$ = 30m, $c_{n',o}$ = 40m, $b_{n',o}$ = 60m, $b_{n',i}$ = 20m, $a_{n',i}$ = 30m, $\theta_{n',i} = \theta_{n',o} = 0°$.

increase in the angular spread is observed. The ratio of heights of far- and local-end scattering clusters is varied and impact on azimuth and elevation AoA PDFs is demonstrated in Fig. 5(c) and 6(c), respectively. The setting of other parameters of MSn for obtaining these graphs is $a_{n,i} = 45$m, $b_{n,i} = 25$m, $a_{n,o} = 75$m, $b_{n,o} = 65$m, $\theta_{n,o} = \theta_{n,i} = 0^o$. The parameter of MS$n'$ are $a_{n',o} = 75$m, $b_{n',o} = 65$m, $a_{n',i} = 45$m, $b_{n',i} = 25$m, $\theta_{n',i} = \theta_{n',o} = 0^o$, and $d = 80$m. The change in dimension of scattering volumes along the vertical axis has a minor impact on PDF of azimuth AoA; however, its impact on the PDF of elevation AoA is significant and important.

The characterization of energy dispersion in the angular domain is important in studying the channel's spatial selective behaviour. Analysis on the spatial spread quantification at both departing and arriving ends of the link in V2V radio propagation environments is conducted in Fig. 7 (a), while observing from MSn. The effect of change in the horizontal

distance d and the ratio between intermediate and major axis of outer boundary of the scattering clusters on the local-end angular spread is plotted in It is observed that with increase in direct distance between MSs, the joint angular spread is increasing. Moreover, angular spread decreases with transformation in the shape of scattering region in x-y plane from circular to elliptical. Characterization of angular constriction in elevation and azimuth planes helps in studying the bias of propagation environment towards two physical directions of arrival and departure. In Fig. 7 (b), Observing from MSn, the effect of variation in link distance and volume of scattering clusters on the elevational constriction shape factor is shown. The effect of change in horizontal distance d and ratio between major axis of far-end and local-end scattering clusters on the azimuthal constriction seen at received side is plotted in Fig. 7 (c). It is observed that the azimuthal constriction increases w.r.t distance up to a certain point, while this trend reverses as decreasing after an increase in the horizontal distance when the far-end's contribution becomes negligible. Similarly, when studying the transmitter side joint angular spread statistics, the effect of change in link distance d and the ratio between intermediate and major axis of the outer boundary is plotted in Fig. 8 (a). The study is further extended to analyze the impact of change in ratio between major axes of local- and far-end scattering clusters in Fig. 8 (c). In Fig. 8 (b), the effect of ratio between the vertical dimension of far- and local-end scattering clusters on the elevational constriction shape factor is demonstrated. The effect is clearly evident with a change in the amount of scatterers along the vertical axis. An increase in the link distance causes an exponential decrease in the elevation constriction of far-end. This is because the prominent two peaks in PDF of AoA transform to conventional PDF of elevational AoA with decreasing value along an the increasing elevation angle.

V. Conclusion

This work has proposed an improved description of the effective scattering clusters in V2V communication environments. Based on the proposed channel model, the AoD and AoA spread has been quantified in terms of the joint angular spread, azimuthal constriction, and the elevational constriction. The proposed channel model, through its flexible description of the geometric shape of scattering clusters, can be used to investigate the effect of various physical channel parameters on the AoD and AoA spreads. The presented analysis is of high significance in enabling the deployment of Massive MIMO in V2V communications. The results are useful for the characterization of Doppler spectrum and for designing optimal beams in vehicular communications.

Acknowledgement

The authors acknowledge the support provided by the EU funded project ATOM-690750 (H2020-MSCA-RISE-2015), Higher Education Commission (HEC) Pakistan funded research project 21-1934 (SRGP-R&D-HEC-18), and travel grant support by HEC Pakistan.

References

[1] S. Kim, D. Kang, and J. Choi, "Beam reconfigurable antenna using switchable parasitic elements for V2V applications," in *proc. of Int. Symp. on Antennas and Propag*, Oct. 2017, pp. 1–2.

[2] Y. Chen, L. Wang, Y. Ai, B. Jiao, and L. Hanzo, "Performance analysis of NOMA-SM in vehicle-to-vehicle massive MIMO channels," *IEEE J. on Selected Areas in Commun.*, vol. 35, no. 12, pp. 2653–2666, 2017.

[3] H. Hartenstein and L. Laberteaux, "A tutorial survey on vehicular ad-hoc networks," *IEEE Commun. Mag.*, vol. 46, no. 6, 2008.

[4] M. Riaz, N. M. Khan, and S. J. Nawaz, "A generalized 3-D scattering channel model for spatiotemporal statistics in mobile-to-mobile communication environment," *IEEE Trans. on Veh. Technol.*, vol. 64, no. 10, pp. 4399–4410, Oct. 2015.

[5] H. Jiang, Z. Zhang, J. Dang, and L. Wu, "A novel 3-D massive MIMO channel model for vehicle-to-vehicle communication environments," *IEEE Trans. on Commun.*, vol. 66, no. 1, pp. 79–90, Jan. 2018.

[6] S. Wu, C. X. Wang, e. H. M. Aggoune, M. M. Alwakeel, and X. H. You, "A general 3D non-stationary 5G wireless channel model," *IEEE Trans. on Commun.*, Dec. 2017.

[7] W. I. Waseer, S. J. Nawaz, S. M. Gulfam, and M. J. Mughal, "Second-order fading statistics of massive-MIMO vehicular radio communication channels," *Trans. on Emerging Tel. Technol., DOI:10.1002/ett.3487*, 2018.

[8] Y. Liu, X. Fang, M. Xiao, and S. Mumtaz, "Decentralized beam pair selection in multi-beam millimeter-wave networks," *IEEE Trans. on Commun.*, vol. 66, no. 6, pp. 2722–2737, Jun 2018.

[9] L. Pang, Y. Zhang, G. Ren, F. Gong, A. Wang, and J. Li, "Markov process based array non-stationarity modeling for massive MIMO channels," in *proc. of Veh. Technol. Conf. (VTC-Fall), 2017*, pp. 1–6.

[10] T. Zwick, C. Fischer, and W. Wiesbeck, "A stochastic multipath channel model including path directions for indoor environments," *IEEE J. on Selected Areas in Commun.*, vol. 20, no. 6, pp. 1178–1192, 2002.

[11] H. Xiao, A. G. Burr, and L. Song, "A time-variant wideband spatial channel model based on the 3GPP model," in *proc. of Veh. Technol. Conf., 2006.*, pp. 1–5.

[12] D. S. Baum, J. Hansen, and J. Salo, "An interim channel model for beyond-3G systems: extending the 3GPP spatial channel model (scm)," in *proc. of Veh. Technol. Conf., 2005.*, vol. 5, pp. 3132–3136.

[13] F. Bohagen, P. Orten, and G. E. Oien, "On spherical vs. plane wave modeling of line-of-sight MIMO channels," *IEEE Trans. on Commun.*, vol. 57, no. 3, pp. 841–849, 2009.

[14] J. Medbo, P. Kyosti, K. Kusume, L. Raschkowski, K. Haneda, T. Jamsa, V. Nurmela, A. Roivainen, and J. Meinila, "Radio propagation modeling for 5G mobile and wireless communications," *IEEE Commun. Mag.*, vol. 54, no. 6, pp. 144–151, 2016.

[15] A. Y. Olenko, K. T. Wong, and E. H.-O. Ng, "Analytically derived ToA-DoA statistics of uplink/downlink wireless multipaths arisen from scatterers on an hollow-disc around the mobile," *IEEE Antennas and Wireless Propag. Lett.*, vol. 2, pp. 345–348, 2003.

[16] B. S. Paul and R. Bhattacharjee, "Time and angle of arrival statistics of mobile-to-mobile communication channel employing dual annular strip model," *IETE J. Research*, vol. 56, no. 6, pp. 327–332, 2010.

[17] S. J. Nawaz, N. M. Khan, M. N. Patwary, and M. Moniri, "Effect of directional antenna on the Doppler spectrum in 3-D mobile radio propagation environment," *IEEE Trans. on Veh. Technol.*, vol. 60, no. 7, pp. 2895–2903, Sep. 2011.

[18] P. Petrus, J. H. Reed, and T. S. Rappaport, "Geometrical-based statistical macrocell channel model for mobile environments," *IEEE Trans. on Commun.*, vol. 50, no. 3, pp. 495–502, Mar. 2002.

[19] A. Ahmed, S. J. Nawaz, and S. M. Gulfam, "A 3-D propagation model for emerging land mobile radio cellular environments," *PLoS ONE*, vol. 10, no. 8, p. e0132555, 2015.

[20] D. G. Valchev, "Spatial modeling of three-dimensional multipath wireless channels," Ph.D. dissertation, 2008.

[21] C. Ziolkowski and J. M. Kelner, "Statistical evaluation of the azimuth and elevation angles seen at the output of the receiving antenna," *IEEE Trans. on Antenna and Propag.*, vol. 66, no. 4, pp. 2165–2169, Apr. 2018.

[22] G. D. Durgin and T. S. Rappaport, "Theory of multipath shape factors for small-scale fading wireless channels," *IEEE Trans. on Antenna and Propag.*, vol. 48, no. 5, pp. 682–693, May 2000.